

Enhanced transverse electron transport via disordered composite formation

Sang J. Park^{1,3,*}, Hojun Lee^{2,*}, Jongjun M. Lee², Jangwoo Ha¹, Hyun-Woo Lee^{2,†} and Hyungyu Jin^{1,‡}

¹*Department of Mechanical Engineering, Pohang University of Science and Technology, Pohang, 37673, South Korea.*

²*Department of Physics, Pohang University of Science and Technology, Pohang, 37673, South Korea.*

³*Present address: National Institute for Materials Science, Tsukuba, 305-0047, Japan.*

Transverse electron transport in magnetic materials — manifested in effects such as the anomalous Hall and Nernst effects — holds promise for spintronic and thermoelectric applications. While recent advances have focused on enhancing such transport through topological single crystals via intrinsic mechanisms linked to Berry curvature, practical limitations remain due to their mechanical fragility and narrow material scope. Here, we demonstrate a distinct approach for transverse transport enhancement based on composite formation. Using both theoretical modeling and experiments, we show that disordered mixtures of two ferromagnetic materials can exhibit significantly stronger transverse electron deflection than either constituent alone. This enhancement originates from meandering electron pathways created by the disordered mixture of two materials and does not rely on long-range crystalline order. The identified requirements for this mechanism can be broadly satisfied across different material systems, offering a universal and tunable strategy to engineer large transverse responses in structurally robust platforms.

Introduction—Transverse transport (TT) in solids [1–6] — where the input and output electron fluxes are orthogonal— enables a wide range of technological applications, including magnetic field sensors [7], transverse thermoelectric generators [8–17], and next-generation spintronics devices [18–20]. By exploiting the unique geometry of TT, it is possible to overcome challenges faced in conventional longitudinal transport, such as limitations in electrical conductivity and the Seebeck effect. For instance, TT can boost the output power of thermoelectric devices by increasing the effective area perpendicular to the input heat flux, thereby eliminating the need for complex electrical contacts and multi-element structures typically required in longitudinal configurations [8,9]. Furthermore, TT offers insights into the physical properties of solids [21–26], deepening our understanding of the complex interplay among charge, spin, and thermal fluxes.

The mechanisms of TT can be classified into intrinsic and extrinsic ones. The intrinsic mechanism [27,28] utilizes the Berry phase, which is determined by energy eigenvalues and eigenstates of a pure material. On the other hand, extrinsic mechanisms (skew scattering mechanism [29] and side-jump mechanism [30]) generate TT through electron scattering by disorders and phonons. The extrinsic contributions are usually smaller than the intrinsic contribution [1,31]. Thus, efforts to strengthen TT have been focused on searching for exotic new materials with large intrinsic contribution. Topological materials are representative candidates of this sort and received great attention [25,32–34]. Alternatively, the extrinsic skew scattering may be utilized to make TT larger than the intrinsic contribution, which is possible in super-clean

materials [35] (materials with exceptionally low longitudinal resistivity). However, super-clean materials are difficult to realize in ambient conditions and thus unsuitable for device applications.

Our approach is different from the above. Our approach enhances TT through composite formation [Fig. 1(a)], which amounts to the physical mixture of two materials. It should be distinguished from the formation of chemical compounds with intermediate chemical composition. Our approach also differs from the aforementioned extrinsic mechanisms in that each constituent material forms domains of its own and maintains its TT, whereas the extrinsic mechanisms modify the TT of individual materials. The central idea of our approach is to form a multi-domain structure of two materials, where each domain is made of one of the two constituent materials. Intuitively, one may expect that the TT of the multi-domain structure is intermediate between those of the two constituent materials, as implied by the effective medium theory [36]. Contrary to this expectation, we show theoretically that the multi-domain structure can exhibit stronger TT than the individual materials. The enhancement is particularly significant when one material with a relatively stronger TT than the other exhibits a relatively weaker longitudinal response than the other. Once this requirement of the material combination is satisfied, this enhancement scheme is applicable to any material combinations. We demonstrate experimentally that this approach can enhance both the anomalous Hall effect (AHE) and the anomalous Nernst effect (ANE) to a level comparable to state-of-the-art single crystalline materials.

* These authors contributed equally to this work.

† Contact author: hwl@postech.ac.kr

‡ Contact author: hgjin@postech.ac.kr

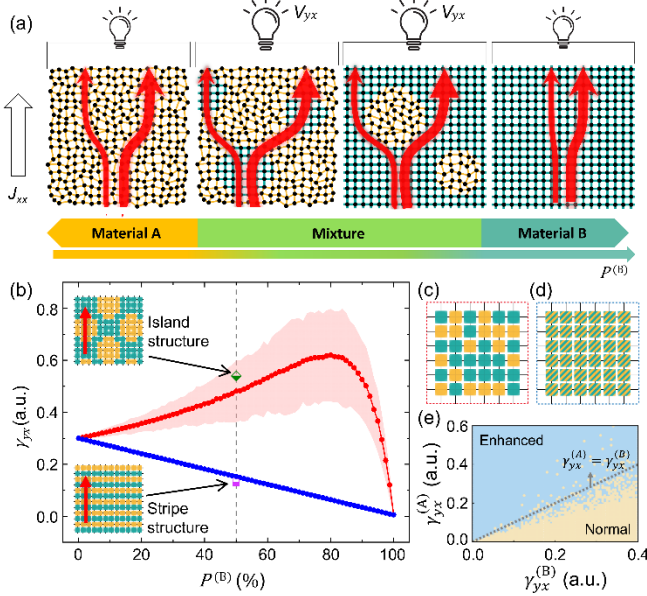


FIG. 1. (a) Schematic of the physical mixture of material A (amorphous, yellow) and B (crystalline, cyan). J_{xx} represents a longitudinal flux. (b) Transverse conductivity γ_{yx} (red symbols and red area) of a random arrangement of A and B domains depicted in (c). The red symbols denote the average $\bar{\gamma}_{yx}$ of γ_{yx} over many random arrangements as a function of the portion of material B ($P^{(B)}$), whereas the red shaded area denotes 1.5- σ (standard deviation) range of γ_{yx} . The blue symbols represent γ_{yx} of the homogeneous network in (d) which consists of a single material with transport properties intermediate between the two materials A and B. The green diamond and purple square represent γ_{yx} at $P^{(B)} = 50\%$ of the island and stripe structure networks, respectively, illustrated in the insets. (e) Diagram showing the $\gamma_{yx}^{(A)}$ and $\gamma_{yx}^{(B)}$ dependence of the enhancement in $\bar{\gamma}_{yx}$. A given combination $(\gamma_{yx}^{(A)}, \gamma_{yx}^{(B)})$ is marked sky blue if the enhancement of $\bar{\gamma}_{yx}$ occurs, and beige if not.

Theoretical model—We demonstrate our strategy by using a network model (Fig. 1; Methods in the Supplemental Material [37], including refs. [8–17,38–62]). Each site is occupied by either material A (lower longitudinal conductivity) with probability $P^{(A)}$ or material B (higher longitudinal conductivity) with probability $P^{(B)}$. To examine charge transport, for instance, the materials A and B at their respective sites are set to have longitudinal conductivities $\gamma_{xx}^{(A)}$ and $\gamma_{xx}^{(B)}$ ($\gamma_{xx}^{(A)} < \gamma_{xx}^{(B)}$) and transverse conductivities $\gamma_{yx}^{(A)}$ and $\gamma_{yx}^{(B)}$, respectively. Here, we use γ to represent the general conductivities. Once the distributions of materials A and B are fixed, the current and voltage profiles are fixed (Methods and Notes S1-S3 in Supplemental Material [37] for details), allowing one to evaluate the longitudinal conductivity γ_{xx} and the transverse conductivity γ_{yx} of the network. For a given value of $P^{(B)}$, networks of randomly

arranged materials A and B are generated many times. For each realization of random arrangement, γ_{xx} and γ_{yx} are evaluated. Figure 1(b) shows the calculation result as a function of $P^{(B)}$. The red dots represent the average $\bar{\gamma}_{yx}$ of γ_{yx} over the realizations and the lightly-red-shaded area denotes the fluctuation range of γ_{yx} . Interestingly, $\bar{\gamma}_{yx}$ depends on $P^{(B)}$ in a nonmonotonic way. In particular, $\bar{\gamma}_{yx}$ at an intermediate $P^{(B)}$ (in the case of Fig. 1(b), $P^{(B)} = 80\%$) is higher than the values of $\bar{\gamma}_{yx}$ at $P^{(B)} = 0\%$ and 100% . This shows that the mixture of two materials can have higher transverse conductivity than each pure material. To determine how generic the mixture-induced enhancement of $\bar{\gamma}_{yx}$ is, we construct the $\bar{\gamma}_{yx}$ vs $P^{(B)}$ diagram as a function of $\gamma_{yx}^{(A)}$ and $\gamma_{yx}^{(B)}$. Figure 1(e) shows its results: a given combination $(\gamma_{yx}^{(A)}, \gamma_{yx}^{(B)})$ is marked sky-blue if the diagram exhibits enhancement at intermediate $P^{(B)}$ and beige if not. Note that sky-blue dots almost completely fill the area in the region with $\gamma_{yx}^{(A)} > \gamma_{yx}^{(B)}$, indicating that the mixture-induced enhancement is quite generic for $\gamma_{yx}^{(A)} > \gamma_{yx}^{(B)}$.

To track down the origin of the enhancement, we consider a few specific networks and calculate their γ_{yx} 's. First, we consider a homogeneous network [Fig. 1(d)], where all sites are occupied by the single material C with its transport properties intermediate between A and B: $\gamma_{xx(yx)}^{(C)} = P^{(A)}\gamma_{xx(yx)}^{(A)} + P^{(B)}\gamma_{xx(yx)}^{(B)}$. The blue dots in Fig. 1(b) show the resulting γ_{yx} as a function of $P^{(B)}$. Note that the blue dots interpolate γ_{yx} 's for $P^{(B)} = 0\%$ and 100% in a monotonic way, which follows the rule of mixtures. This result implies that for the *physical* mixture-induced enhancement [Fig. 1(b), red dots] to occur, each site should keep the properties of either material A or B (instead of intermediate properties). That is, the mixture-induced enhancement originates from the physical mixture. Next, we consider the network, where materials A and B form stripe structures (Fig. 1(b), lower inset), and the network, where material A forms islands embedded in material B (Fig. 1(b), upper inset). $P^{(B)}$ is set to 50% for both networks. γ_{yx} for the stripe structure network is close to γ_{yx} for the homogeneous network at $P^{(B)} = 50\%$, which indicates that the physical mixture alone does not guarantee the enhancement. On the other hand, γ_{yx} for the island structure network is close to $\bar{\gamma}_{yx}$ for the randomly generated inhomogeneously populated network (red dots). Thus, the mixture-induced enhancement occurs in the island structure network. To clarify the core difference between the stripe structure network and the island structure network, we calculate γ_{yx} for additional structures and find that the enhancement occurs when the physical mixture makes charge current paths *meandering*. In the island structure, for instance, the current paths tend to stay within the cyan region (region occupied by material B) and form meandering paths simply because the longitudinal

conductivity at each site is larger for domain B than domain A ($\gamma_{xx}^{(A)} < \gamma_{xx}^{(B)}$). Thus, the longitudinal conductance difference combined with the physical mixture generates trajectory “side-jump”s of island size (Fig. 1(a), third panel, Fig. S2(a)-(c), Note S2 in Supplemental Material [37]) even without the action of the transverse conductivities, $\gamma_{yx}^{(A)}$ and $\gamma_{yx}^{(B)}$. The role of $\gamma_{yx}^{(A)}$ and $\gamma_{yx}^{(B)}$ is to break the balance between left and right side-jump trajectories. In particular, the enhancement condition $\gamma_{yx}^{(A)} > \gamma_{yx}^{(B)}$ [Fig. 1(e)] implies that the balance breaking is caused near the sites where straight segments of the current paths encounter islands of material A. This asymmetric side jump generates additional transverse flows, which causes the enhancement. A similar enhancement occurs when materials A and B sites are swapped (Fig. 1(a), second panel, Fig. S2(d)-(f), Note S2 in Supplemental Material [37]). In this case, the current paths tend to minimize the portion in material A, which generates trajectory side-jumps. In the stripe structure network, in contrast, the physical mixture does not generate the trajectory side-jump, and thus the mixture-induced enhancement is not significant there. However, in randomly generated networks, networks similar to the stripe structure network are extremely unlikely and almost all networks have meandering current paths, which indicates that the mixture-induced enhancement is quite generic if the condition $\gamma_{yx}^{(A)} > \gamma_{yx}^{(B)}$ is satisfied. In real materials formed by a physical mixture of materials A and B (e.g., composites), it is also highly likely that microstructures resembling the randomly generated networks are formed. Therefore, we put forward that the proposed strategy is applicable to a wide range of materials.

Experimental system: Ferromagnetic metallic glasses with controlled phase domains—We now introduce the experimental system for the test of the theoretical prediction. We chose ferromagnetic metallic glasses of composition $\text{Fe}_{92.5}\text{Si}_5\text{B}_{2.5}$ as the test system, where the proportion of heterostructures (i.e., crystalline phase vs. amorphous phase) can be systematically adjusted by varying the annealing temperature T_a (Fig. 2). The two phases may be regarded as two different materials for our purpose. The amorphous phase has lower longitudinal (higher transverse) conductivity than the crystalline phase, as confirmed in Fig. 3(c) (Fig. 3(d)). A composite that consists of domains of the two phases can render a system that satisfies the predicted requirement for the enhancement. Two sets of samples were prepared for validation with two different annealing times: 1 h and 5 min. While both sets clearly demonstrated the validity of the model with enhanced TT properties at mild T_a , we focus on the 1-h annealed set in the main text, as it exhibits more distinct crystalline-amorphous domain distributions without the formation of metastable phases. Accordingly, unless otherwise noted, the data presented in the following sections correspond to the 1-h annealed set.

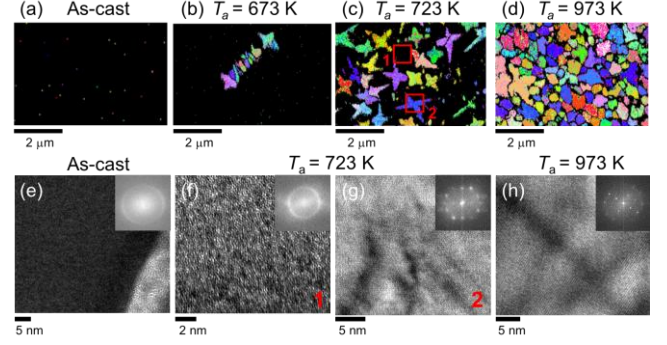


Fig. 2. Color mapping images of crystalline phases measured using SEM in (a) as-cast, (b) $T_a=673$ K, (c) $T_a=723$ K, and (d) $T_a=973$ K samples. TEM images and corresponding diffraction patterns of (e) amorphous (as-cast), (f, g) partially crystallized ($T_a=723$ K), and (h) poly-crystalline ($T_a=973$ K) samples. (f) and (g) were obtained at amorphous and crystalline spots in the same $T_a = 723$ K sample, given in (c).

The TT data from the 5-min annealed set are provided in Fig. S3 in Supplemental Material [37].

To systematically explore the influence of domain distribution on TT, we selected five representative T_a of 673, 698, 723, 773, and 973 K with an unannealed (as-cast) sample for reference (Methods in Supplemental Material [37]). Electron backscattered diffraction imaging revealed an increase in the crystalline fraction with rising T_a [Figs. 2(a)-2(d)]. In the $T_a=673$ K sample, multiphase grain islands began crystallizing with increasing T_a [63,64]. The $T_a=973$ K sample was observed to be nearly fully crystallized. The evolution of sample morphology with varying T_a was further corroborated using transmission electron microscopy (TEM) [Figs. 2(e)-2(h)]. Low-magnification TEM images of the $T_a=723$ K sample distinctly showed dendritic structures (Fig. S4 in Supplemental Material [37]). Selected area diffraction patterns indicated a gradual transition from amorphous (as-cast) to crystalline ($T_a=973$ K). We find that the $T_a=723$ K sample exhibits a heterostructure that resembles the island structure network in our theoretical model [Fig. 1(b), inset]. Overall, we confirm that the intended sample set is successfully constructed, wherein the ratio between amorphous and crystalline domains is systematically varied with T_a . Material characterization details are provided in Figs. S4-S6 and Note S3 of the Supplemental Material [37].

Experimental validation of network model via transport measurements—We now present experimental evidence of enhanced TT in random physical mixtures of amorphous and crystalline domains that supports our theoretical network model (Fig. 3, Methods in Supplemental Material [37]). Figures 3(c) and 3(d) show that the amorphous as-cast sample possesses a lower longitudinal electrical conductivity ($\sigma_{xx}=8.28 \times 10^3$ S/cm at $T=300$ K) and a higher transverse anomalous Hall conductivity ($|\sigma_{yx}|=467$ S/cm, where $\sigma_{yx} =$

$-\rho_{yx}/(\rho_{xx}^2 + \rho_{yx}^2)$) compared to its crystalline counterpart ($\sigma_{xx}=15.6 \times 10^3$ S/cm and $|\sigma_{yx}|=155$ S/cm for $T_a=973$ K). Here, x and y represent the directions of applied charge (I) or heat current (Q) and measured transverse voltage, respectively, following the sign convention in [13] (Fig. 3(a) and Fig. S7). We note that this satisfies the condition for the occurrence of enhanced TT in our network model. As a result, the enhanced TT is clearly observed in the samples with island-like heterostructures at 300 K [Fig. 3(d)] with T -dependence provided in Fig. S8 in Supplemental Material [37]; σ_{yx} peaks at $T_a=723$ K ($|\sigma_{yx}|=780$ S/cm at $T=300$ K), significantly exceeding the values for both amorphous (i.e., as-cast) and crystalline (i.e., $T_a=973$ K) samples.

The non-monotonic dependence of σ_{yx} on T_a contrasts with the near monotonic dependence of σ_{xx} , revealing the more sensitive nature of TT to the microscopic domain distribution than its longitudinal counterpart. Notably, $|\sigma_{yx}|=780$ S/cm for the $T_a=723$ K sample corresponds to as much as ~ 5 -fold enhancement compared to that for the crystalline ($T_a=973$ K) sample. Such strong enhancement leads to an impressive anomalous Hall angle (AHA= $|\frac{\sigma_{yx}}{\sigma_{xx}}| \times 100\%$) of 6.7%, which is even larger than those of Fe-based single crystalline Fe_3Ga and Fe_3Al ($|\sigma_{yx}|=440\text{--}540$ S/cm and AHA=3.7–5.1% at

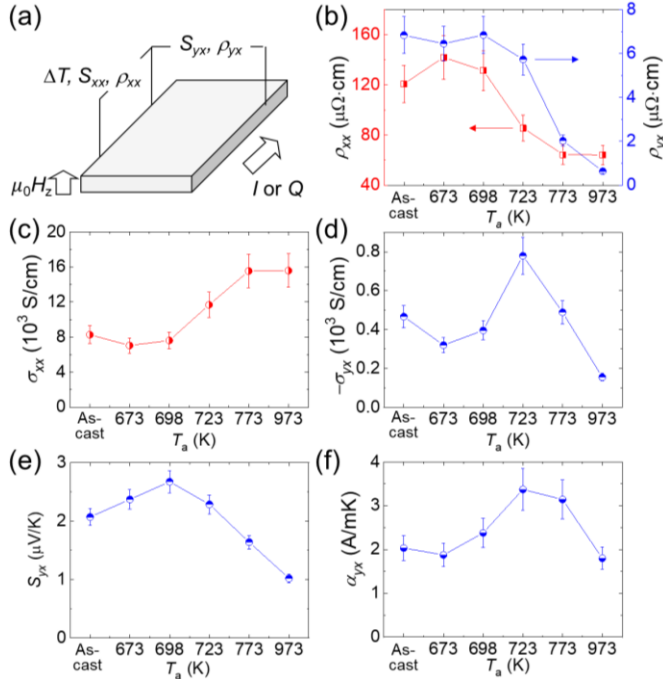


Fig. 3. (a) Measurement schematic of transport properties in response to longitudinal electrical (I) and thermal (Q) fluxes. (b) Longitudinal electrical resistivity (ρ_{xx}) and anomalous Hall resistivity (ρ_{yx}) as a function of annealing temperature (T_a). (c) Longitudinal electrical conductivity (σ_{xx}) and (d) anomalous Hall conductivity (σ_{yx}). (e) Anomalous Nernst coefficient (S_{yx}) and (f) anomalous Nernst conductivity (α_{yx}). All properties were measured at $T=300$ K.

$T=300$ K) [11], despite the much smaller amount of secondary elements used in our materials ($\text{Fe}_{92.5}\text{Si}_5\text{B}_{2.5}$). Note that before the enhancement, the AHA of our crystalline ($T_a=973$ K) sample is merely 0.99%.

Enhanced TT is also consistently observed in the thermal transport represented by ANE at 300 K (See Figs. S8 and S9 and Note S5 for T -dependent data and thermal conductivity of 1-h annealed set, respectively, and Fig. S3 for 5-min annealed set). The anomalous Nernst coefficient (S_{yx}) shows a similar behavior with σ_{yx} , where the heterostructure samples outperform their amorphous and crystalline counterparts [Fig. 3(e) and Fig. S3(a)]. S_{yx} increases with T_a within the sample set annealed for 1 h (5 min), reaching 2.67 $\mu\text{V/K}$ (3.69 $\mu\text{V/K}$) for the heterostructure sample with $T_a=698$ K ($T_a=773$ K) before diminishing to 0.97 $\mu\text{V/K}$ for the $T_a=973$ K crystalline sample. The enhanced S_{yx} values in the heterostructure samples are one order higher than that of α -Fe single crystals (~ 0.3 $\mu\text{V/K}$). Considering the composition of our samples is $\text{Fe}_{92.5}\text{Si}_5\text{B}_{2.5}$, where Fe is the major constituent element, it is remarkable that the manipulation of domain structure with a small fraction of Si and B substitution can lead to such a significant enhancement in S_{yx} . We also evaluated the anomalous Nernst conductivity ($\alpha_{yx} = S_{xx}\sigma_{yx} + S_{yx}\sigma_{xx}$), a pivotal TT parameter that directly connects longitudinal temperature gradient with transverse electric current [Fig. 3(f) and Fig. S3(b)] [65–67]. The largest value of 3.37 A/(m·K) (4.94 A/(m·K)) is shown by the $T_a=723$ K ($T_a=773$ K) heterostructure sample annealed for 1 h (5 min), which corresponds approximately to double (triple) that of the $T_a=973$ K crystalline sample (1.72 A/(m·K)). The observed α_{yx} values are comparable and even larger than those of state-of-the-art single crystals such as Co_2MnGa (3–3.4 A/(m·K)) [12,53,57] and Fe_3Ga (4.49–4.83 A/(m·K)) [11], whose large α_{yx} values are attributed to intrinsic band topology.

In addition to the enhancement of various TT coefficients, the peak location of $T_a=723$ K (or 698 K) also supports our theoretical prediction. According to our theoretical model, the TT is enhanced in the parameter range (T_a is the relevant parameter in our experimental situation) where straight current paths are suppressed and replaced by meandering paths (2nd and 3rd panels in Fig. 1(a)). In our experiment, σ_{xx} changes rapidly near $T_a=723$ K from its crystalline value to the amorphous value, and thus meandering paths should be most pronounced near $T_a=723$ K, which is the location where TT is enhanced in agreement with the theoretical prediction. This observation is consistent with the microscopic structure observation where the $T_a=723$ K sample shows the distinct island-like crystalline phase domains in the amorphous matrix [Fig. 2(c)]. We further investigate whether the strong enhancement of σ_{yx} , S_{yx} , and α_{yx} in our heterostructure samples can be explained by other mechanisms. We specifically consider the case of σ_{yx} which has been extensively studied over past decades [1,35,66]. When the

intrinsic Berry curvature mechanism is the dominant source of σ_{yx} , σ_{yx} should be independent of σ_{xx} [68]. On the other hand, when the extrinsic mechanisms such as the skew scattering mechanism [69] or the side jump mechanism [30] is the dominant source of σ_{yx} , σ_{yx} should be proportional to σ_{xx} or independent of σ_{xx} , respectively. Comparison between experimental σ_{xx} and σ_{yx} [Figs. 3(c) and 3(d)] indicates that neither of the relations is satisfied, implying that the enhancement of TT in our experiment is not due to the conventional mechanisms (additional information in Notes S6 and S7, and Figs. S10-S14 in Supplemental Material [37]). In contrast, our theoretical model naturally explains the peak formation of σ_{yx} in the region where σ_{xx} changes rapidly. We thus believe that our mechanism provides a convincing explanation for the observed σ_{yx} enhancement in our heterostructure samples, wherein amorphous and crystalline phases (as if they are two different materials) are physically mixed.

Overall, the experimental results strongly support the theoretical prediction of the network model. The clear dependency of AHE and ANE on T_a and the corresponding microscopic structure suggests that the dominant source responsible for the enhancement is the formation of island-like domains, which leads to meandering current paths. A recent experiment reported that nanostructure engineering can mysteriously enhance the transverse thermoelectric conversion [70]. Since the nanostructure engineering leads to the composite formation similar to our experimental system, we argue that our mechanism provides an explanation to the reported enhancement. Such consistent observations in different material systems corroborate the universal applicability of our enhancement scheme across broad material classes and their combinations.

Conclusions—The universality of the proposed approach essentially arises from its independence from specific material parameters in our theoretical model, such as crystallographic orientation and electronic band structure. The approach in principle can be applied to any physical mixtures of two materials that satisfy the following requirements: 1) satisfying inequalities in the longitudinal and transverse conductivities between material A and B (i.e.,

$\gamma_{xx}^{(A)} < \gamma_{xx}^{(B)}$ and $\gamma_{yx}^{(A)} > \gamma_{yx}^{(B)}$), and 2) forming hetero-domains that give rise to meandering current paths. This allows the creation of new materials with large TT by mixing already existing materials. When this enhancement scheme is applied to a combination that includes state-of-the-art materials, there is a possibility to go even beyond the state-of-the-art TT. Furthermore, occasional discoveries of new material classes will provide opportunities to create new large TT materials using the proposed approach.

While we exemplified our approach with the well-known anomalous Hall and Nernst effects in electronic systems, we expect that our approach can be applied to enhance the transverse transport of various kinds of flux. For example, it may be applied to the transverse transport of an ionic flux, such as the ionic Hall effect in heterogeneous composites consisting of ionic conductors. Therefore, our approach may contribute to developing novel device applications based on transverse transport of different kinds of flux. Lastly, the materials created by the proposed approach will be non-single crystalline, which offers practical advantages over single crystalline materials such as better mechanical stability and lower fabrication cost.

Acknowledgments—The authors thank Proterial Korea, Ltd. for providing the commercial amorphous metals (2605SA1) for research purposes. The authors thank Ki Mun Bang for help with figures and Ji-Hyun Seong, Ho-Jun Gang, Jung-Hun Kim, and Eun-Ho Lee for their technical support. This work was supported by Samsung Research Funding & Incubation Center of Samsung Electronics under Project Number SRFC-MA2002-02, National Research Foundation of Korea (NRF) grant funded by the Korea government (MSIT) RS-2024-00345022 and No. NRF-2022M3C1A3091988, Samsung Science and Technology Foundation grant BA-1501-51, National Research Foundation of Korea (NRF) grant funded by the Korean government (MSIT) RS-2024-00410027, and National Supercomputing Center with supercomputing resources including technical support (KSC-2022-CRE-0468).

- [1] N. Nagaosa, J. Sinova, S. Onoda, A. H. MacDonald, and N. P. Ong, Anomalous Hall effect, *Rev Mod Phys* **82**, 1539 (2010).
- [2] J. Sinova, S. O. Valenzuela, J. Wunderlich, C. H. Back, and T. Jungwirth, Spin Hall effects, *Rev Mod Phys* **87**, 1213 (2015).
- [3] K. von Klitzing et al., 40 years of the quantum Hall effect, *Nature Reviews Physics* **2**, 397 (2020).
- [4] C. Z. Chang, C. X. Liu, and A. H. Macdonald, Colloquium: Quantum anomalous Hall effect, *Rev Mod Phys* **95**, 011002 (2023).
- [5] G. E. W. Bauer, E. Saitoh, and B. J. Van Wees, Spin caloritronics, *Nat Mater* **11**, 391 (2012).
- [6] S. R. Boona, R. C. Myers, and J. P. Heremans, Spin caloritronics, *Energy Environ Sci* **7**, 885 (2014).
- [7] S. Tumanski, Modern magnetic field sensors – a review, *Przeglad Elektrotechniczny* **89**, 1 (2013).
- [8] K. Uchida and J. P. Heremans, Thermoelectrics: From longitudinal to transverse, *Joule* **6**, 2240 (2022).
- [9] S. R. Boona, H. Jin, and S. Watzman, Transverse thermal energy conversion using spin and topological structures, *J Appl Phys* **130**, 171101 (2021).
- [10] M. Ikhlas, T. Tomita, T. Koretsune, M. T. Suzuki, D. Nishio-Hamane, R. Arita, Y. Otani, and S. Nakatsuji, Large anomalous Nernst effect at room

- temperature in a chiral antiferromagnet, *Nat Phys* **13**, 1085 (2017).
- [11] A. Sakai et al., Iron-based binary ferromagnets for transverse thermoelectric conversion, *Nature* **581**, 53 (2020).
 - [12] A. Sakai et al., Giant anomalous Nernst effect and quantum-critical scaling in a ferromagnetic semimetal, *Nat Phys* **14**, 1119 (2018).
 - [13] Y. Pan, C. Le, B. He, S. J. Watzman, M. Yao, J. Gooth, J. P. Heremans, Y. Sun, and C. Felser, Giant anomalous Nernst signal in the antiferromagnet YbMnBi_2 , *Nat Mater* **21**, 203 (2022).
 - [14] B. He, C. Şahin, S. R. Boona, B. C. Sales, Y. Pan, C. Felser, M. E. Flatté, and J. P. Heremans, Large magnon-induced anomalous Nernst conductivity in single-crystal MnBi , *Joule* **5**, 3057 (2021).
 - [15] C. Fu et al., Large Nernst power factor over a broad temperature range in polycrystalline Weyl semimetal NbP , *Energy Environ Sci* **11**, 2813 (2018).
 - [16] S. N. Guin et al., Zero-Field Nernst Effect in a Ferromagnetic Kagome-Lattice Weyl-Semimetal $\text{Co}_3\text{Sn}_2\text{S}_2$, *Advanced Materials* **31**, 1806622 (2019).
 - [17] W. Zhou, K. Yamamoto, A. Miura, R. Iguchi, Y. Miura, K. Uchida, and Y. Sakuraba, Seebeck-driven transverse thermoelectric generation, *Nat Mater* **20**, 463 (2021).
 - [18] A. Hirohata, K. Yamada, Y. Nakatani, L. Prejbeanu, B. Diény, P. Pirro, and B. Hillebrands, Review on spintronics: Principles and device applications, *J Magn Mater* **509**, 166711 (2020).
 - [19] B. Dieny et al., Opportunities and Challenges for Spintronics in the Microelectronics Industry, *Nat Electron* **3**, 446 (2020).
 - [20] S. J. Park et al., Enhancing spin pumping by nonlocal manipulation of magnon temperature, *Matter* **7**, 4332 (2024).
 - [21] L. Fu and C. L. Kane, Topological insulators with inversion symmetry, *Phys Rev B Condens Matter Mater Phys* **76**, 045302 (2007).
 - [22] L. Zhang, J. Ren, J. S. Wang, and B. Li, Topological nature of the phonon Hall effect, *Phys Rev Lett* **105**, 225901 (2010).
 - [23] J. Cai et al., Signatures of fractional quantum anomalous Hall states in twisted MoTe_2 , *Nature* **622**, 63 (2023).
 - [24] Y. Onose, T. Ideue, H. Katsura, Y. Shiomi, N. Nagaosa, and Y. Tokura, Observation of the magnon Hall effect, *Science* **329**, 297 (2010).
 - [25] C. L. Kane and E. J. Mele, \mathbb{Z}_2 topological order and the quantum spin Hall effect, *Phys Rev Lett* **95**, 146802 (2005).
 - [26] H. Katsura, N. Nagaosa, and P. A. Lee, Theory of the thermal Hall effect in quantum magnets, *Phys Rev Lett* **104**, 066403 (2010).
 - [27] R. Karplus and J. M. Luttinger, Hall Effect in Ferromagnetics, *Phys Rev* **95**, 1154 (1954).
 - [28] T. Jungwirth, Q. Niu, and A. H. MacDonald, Anomalous Hall Effect in Ferromagnetic Semiconductors, *Phys Rev Lett* **88**, 207208 (2002).
 - [29] J. Smit, The spontaneous hall effect in ferromagnetics II, *Physica* **24**, 39 (1958).
 - [30] L. Berger, Side-Jump Mechanism for the Hall Effect of Ferromagnets, *Physics Review B* **2**, 4559 (1970).
 - [31] D. Xiao, M. C. Chang, and Q. Niu, Berry phase effects on electronic properties, *Rev Mod Phys* **82**, 1959 (2010).
 - [32] F. D. M. Haldane, Berry Curvature on the Fermi Surface: Anomalous Hall Effect as a Topological Fermi-Liquid Property, *Phys Rev Lett* **93**, 206602 (2004).
 - [33] M. König, S. Wiedmann, C. Brüne, A. Roth, H. Buhmann, L. W. Molenkamp, X.-L. Qi, and S.-C. Zhang, Quantum Spin Hall Insulator State in HgTe Quantum Wells, *Science* **318**, 766 (1980).
 - [34] C.-Z. Chang et al., Experimental Observation of the Quantum Anomalous Hall Effect in a Magnetic Topological Insulator, *Science* **340**, 167 (2013).
 - [35] S. Onoda, N. Sugimoto, and N. Nagaosa, Quantum transport theory of anomalous electric, thermoelectric, and thermal Hall effects in ferromagnets, *Phys Rev B* **77**, 165103 (2008).
 - [36] D. J. Bergman and O. Levy, Thermoelectric properties of a composite medium, *J Appl Phys* **70**, 6821 (1991).
 - [37] See the Supplemental Material at [LINK] for additional information, including details on the theoretical model, network size dependence, structural characterization of the samples (via in-situ X-ray diffraction, differential scanning calorimetry, and TEM), temperature-dependent transport properties, and thermoelectric simulations in composite materials.
 - [38] J. Medina, D. Green, and C. Chamon, Networks of quantum wire junctions: A system with quantized integer Hall resistance without vanishing longitudinal resistivity, *Phys Rev B Condens Matter Mater Phys* **87**, 045128 (2013).
 - [39] J. M. Lee, M. Oshikawa, and G. Y. Cho, Non-Fermi Liquids in Conducting Two-Dimensional Networks, *Phys Rev Lett* **126**, 186601 (2021).
 - [40] K. M. Bang, S. J. Park, H. Yu, and H. Jin, Large transverse thermopower in shape-engineered tilted leg thermopile, *Appl Energy* **368**, 123222 (2024).
 - [41] W. Minor, B. Schonfeld, B. Lebeck, B. Buras, and W. Dmowski, Crystallization of Fe-Si-B metallic glasses studied by X-ray synchrotron radiation, *J Mater Sci* **22**, 4144 (1987).
 - [42] M. E. McHenry, F. Johnson, H. Okumura, T. Ohkubo, V. R. V. Ramanan, and D. E. Laughlin, The kinetics of nanocrystallization and microstructural

- observations in FINEMET, NANOPERM and HITPERM nanocomposite magnetic materials, *Scr Mater* **48**, 881 (2003).
- [43] S. Zhou, B. Dong, R. Xiang, G. Zhang, J. Qin, and X. Bian, Influence of clusters in melt on the subsequent glass-formation and crystallization of Fe-Si-B metallic glasses, *Progress in Natural Science: Materials International* **25**, 137 (2015).
- [44] H. Tanimoto, R. Hozumi, and M. Kawamura, Electrical resistivity and short-range order in rapid-quenched CrMnFeCoNi high-entropy alloy, *J Alloys Compd* **896**, 163059 (2022).
- [45] L. Li, Z. Chen, S. Kuroiwa, M. Ito, K. Yuge, K. Kishida, H. Tanimoto, Y. Yu, H. Inui, and E. P. George, Evolution of short-range order and its effects on the plastic deformation behavior of single crystals of the equiatomic Cr-Co-Ni medium-entropy alloy, *Acta Mater* **243**, 118537 (2023).
- [46] A. Manzoor Rana, A. Faheem Khan, A. Abbas, and M. I. Ansari, Electrical resistivity behavior in Ni-25 at.% Cr alloy, *Mater Chem Phys* **80**, 228 (2003).
- [47] S. J. Watzman, R. A. Duine, Y. Tserkovnyak, S. R. Boona, H. Jin, A. Prakash, Y. Zheng, and J. P. Heremans, Magnon-drag thermopower and Nernst coefficient in Fe, Co, and Ni, *Phys Rev B* **94**, 144407 (2016).
- [48] V. Dobrosavljevic, T. R. Kirkpatrick, and G. Kotliar, Kondo Effect in Disordered Systems, *Phys Rev Lett* **69**, 1113 (1992).
- [49] A. Molinari et al., Disorder-Induced Magnetotransport Anomalies in Amorphous and Textured Co_{1-x}Si_x Semimetal Thin Films, *ACS Appl Electron Mater* **5**, 2624 (2023).
- [50] X. Li et al., Large and robust charge-to-spin conversion in sputtered conductive WTex with disorder, *Matter* **4**, 1639 (2021).
- [51] H. Z. Lu and S. Q. Shen, Weak antilocalization and localization in disordered and interacting Weyl semimetals, *Phys Rev B Condens Matter Mater Phys* **92**, 035203 (2015).
- [52] P. A. Lee and T. V Ramakrishnan, Disordered electronic systems, *Rev Mod Phys* **57**, 287 (1985).
- [53] S. N. Guin et al., Anomalous Nernst effect beyond the magnetization scaling relation in the ferromagnetic Heusler compound Co₂MnGa, *NPG Asia Mater* **11**, 16 (2019).
- [54] F. Mende, J. Noky, S. N. Guin, G. H. Fecher, K. Manna, P. Adler, W. Schnelle, Y. Sun, C. Fu, and C. Felser, Large Anomalous Hall and Nernst Effects in High Curie-Temperature Iron-Based Heusler Compounds, *Advanced Science* **8**, 2100782 (2021).
- [55] W. X. Zhou, Y. Cheng, K. Q. Chen, G. Xie, T. Wang, and G. Zhang, Thermal Conductivity of Amorphous Materials, *Adv Funct Mater* **30**, 1903829 (2020).
- [56] W. Zhou and Y. Sakuraba, Heat flux sensing by anomalous Nernst effect in Fe-Al thin films on a flexible substrate, *Applied Physics Express* **13**, 043001 (2020).
- [57] L. Xu, X. Li, L. Ding, T. Chen, A. Sakai, B. Fauqué, S. Nakatsuji, Z. Zhu, and K. Behnia, Anomalous transverse response of Co₂MnGa and universality of the room-temperature $\alpha_{ij}A / \sigma_{ij}A$ ratio across topological magnets, *Phys Rev B* **101**, 180404(R) (2020).
- [58] L. Ding et al., Intrinsic Anomalous Nernst Effect Amplified by Disorder in a Half-Metallic Semimetal, *Phys Rev X* **91**, 041061 (2019).
- [59] R. A. Secco, Thermal conductivity and Seebeck coefficient of Fe and Fe-Si alloys: Implications for variable Lorenz number, *Physics of the Earth and Planetary Interiors* **265**, 23 (2017).
- [60] C. L. Hsin, Y. T. Liu, and Y. Y. Tsai, Suppressed Umklapp scattering of β -FeSi₂ thin film and single crystalline nanowires, *Nanotechnology* **28**, 485702 (2017).
- [61] B. Buschinger, C. Geibel, F. Steglich, D. Mandrus, D. Young, J. L. Sarrao, and Z. Fisk, Transport properties of FeSi, *Physica B* **230–232**, 784 (1997).
- [62] Y. Hamada, Y. Kurokawa, T. Yamauchi, H. Hanamoto, and H. Yuasa, Anomalous Nernst effect in Fe-Si alloy films, *Appl Phys Lett* **119**, 152404 (2021).
- [63] Y. R. Zhang and R. V. Ramanujan, The effect of niobium alloying additions on the crystallization of a Fe-Si-B-Nb alloy, *J Alloys Compd* **403**, 197 (2005).
- [64] S. G. Kim, N. E. Lee, and H. Y. Ra, Dendritic growth of a(Fe,Si) ferrite in annealed Fe₈₀Si₈B₁₂ metallic glass, *J Cryst Growth* **92**, 629 (1988).
- [65] W. Zhou, A. Miura, Y. Sakuraba, and K. I. Uchida, Direct Electrical Probing of Anomalous Nernst Conductivity, *Phys Rev Appl* **19**, 064079 (2023).
- [66] T. Miyasato, N. Abe, T. Fujii, A. Asamitsu, S. Onoda, Y. Onose, N. Nagaosa, and Y. Tokura, Crossover behavior of the anomalous Hall effect and anomalous Nernst effect in itinerant ferromagnets, *Phys Rev Lett* **99**, 086602 (2007).
- [67] D. Xiao, Y. Yao, Z. Fang, and Q. Niu, Berry-phase effect in anomalous thermoelectric transport, *Phys Rev Lett* **97**, 026603 (2006).
- [68] R. Karplus and J. M. Luttinger, Hall Effect in Ferromagnetics, *Physics Review* **95**, 1154 (1954).
- [69] L. C. Hebel and G. E. Smith, Interband transitions and band structure of a BiSb alloy, *Physics Letters* **10**, 273 (1958).
- [70] R. Gautam, T. Hirai, A. Alasli, H. Nagano, T. Ohkubo, K. Uchida, and H. Sepehri-Amin, Creation of flexible spin-caloritronic material with giant transverse thermoelectric conversion by

nanostructure engineering, Nat Commun **15**, 2184 (2024).